

An Optics-Free Ultra-Thin Time-Resolved Intraoperative Imaging Platform for Deep Infrared Imaging of Alloyed Upconverting Nanoparticles

Hossein Najafiaghdam

Electrical Engineering and Computer Sciences
University of California at Berkeley

Technical Report No. UCB/EECS-2019-20

<http://www2.eecs.berkeley.edu/Pubs/TechRpts/2019/EECS-2019-20.html>

May 1, 2019



Copyright © 2019, by the author(s).
All rights reserved.

Permission to make digital or hard copies of all or part of this work for personal or classroom use is granted without fee provided that copies are not made or distributed for profit or commercial advantage and that copies bear this notice and the full citation on the first page. To copy otherwise, to republish, to post on servers or to redistribute to lists, requires prior specific permission.

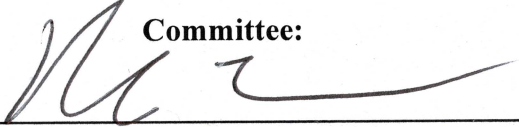
An Optics-Free Ultra-Thin Time-Resolved Intraoperative Imaging Platform for Deep Infrared Imaging of Alloyed Upconverting Nanoparticles

by Hossein Najafiaghdam

Research Project

Submitted to the Department of Electrical Engineering and Computer Sciences, University of California at Berkeley, in partial satisfaction of the requirements for the degree of **Master of Science, Plan II.**

Approval for the Report and Comprehensive Examination:

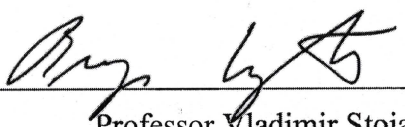

Committee:

Professor Mekhail Anwar
Research Advisor

12/11/18

(Date)

* * * * *



Professor Vladimir Stojanovic
Second Reader

12/8/2018

(Date)

Abstract

An Optics-Free Ultra-Thin Time-Resolved Intraoperative Imaging Platform for Deep Infrared
Imaging of Alloyed Upconverting Nanoparticles

By

Hossein Najafiaghdam

Master of Advanced Study in Integrated Circuits

Electrical Engineering and Computer Science

University of California, Berkeley

Professor Ali Niknejad and Mekhail Anwar

Microscopic tumor foci are often left behind in the surgical bed during cancer surgery, increasing cancer recurrence. Despite the introduction of fluorescently-tagged targeted molecular imaging agents, molecularly guided cancer surgeries remain hindered by imagers themselves. The bulky and rigid optical lenses and filters, required to resolve the weak fluorescence signal from background, are challenging to miniaturize, and restrict the imager to relatively far from the tumor cells, reducing both the sensitivity and maneuverability within complex tumor cavities. Ideal molecular imaging systems require ultra-small form-factor devices high sensitivity (<5000 cells) for microscopic margin imaging, and deep IR penetration lymph node imaging.

We shift the cumbersome optical requirements of fluorescence imaging into the time domain, using an optics-free micro-fabricated, time-resolved contact imaging array. Made possible through the synergistic integration of a custom high-speed integrated circuit imaging array and biocompatible PEG-coated alloyed upconverting nanoparticles (aUCNPs), which are 2-3 orders of magnitude brighter than conventional lanthanide-doped UCNPs and have long ($>100\mu\text{s}$) phosphorescence lifetimes, this work provides the proof of concept and a $200\mu\text{m}$ -thin imager, which functions as a scalable molecular imaging skin, able to be integrated on any surgical instrument, for real-time, visualization of tumor cells intraoperatively. Using time-resolving imaging, we alternate pulses of excitation light (980nm and 1550nm wavelengths) with light sensing, taking advantage of the aUCNP's emission lifetime. Using power levels compatible with *in vivo* use, we achieve cell-level detection of spatial features.

To assess bio-distribution of the aUCNPs, injected mammary glands were imaged with an excitation power of only $0.1\text{W}/\text{cm}^2$ at 980nm, showing the particles still remained in the gland even hours after injection, making time-resolved imaging possible during surgery with the current imager.

Table of Contents

1	Introduction	4
1.1	Motivation	4
1.2	Challenges	5
1.3	Objectives	6
2	Fluorescence Imaging	7
2.1	Frequency domain resolution	7
2.1.1	Concept	7
2.1.2	Challenges	7
2.2	Time-domain resolution	8
2.2.1	Concept	8
2.2.2	Challenges	9
3	Alloyed Upconverting Nanoparticles	10
3.1	Emission decay	11
3.2	Upconversion efficiency	13
3.3	Excitation duration	14
4	Imaging Platform and Experimental Image Acquisition	16
4.1	Concentrated aUCNP vial	16
4.2	aUCNP-coated Polydimethylsiloxane (PDMS) Micro-well	17
5	Animal Trial and Bio-distribution	19
6	Future work and conclusion	21
	Bibliography	22

Table of Figures

Figure 1. Effects of MRD on cancer recurrence rates.....	4
Figure 2. Time domain image resolution diagram.....	8
Figure 3. Experiment setup for aUCNP characterization.	10
Figure 4. Measured emission intensity decay of aUCNPs (dark current subtracted and $T_{exc} = 5ms$): (a) At 8 W/cm ² of 980nm excitation. (b) At 60 W/cm ² of 1550nm excitation.	11
Figure 5. Measured integrated emission intensity of aUCNPs ($T_{exc} = 5ms$): (a) At 8 W/cm ² of 980nm excitation. (b) At 60 W/cm ² of 1550nm excitation.	12
Figure 6. Measured emission intensity of aUCNPs at different power levels ($T_{int} = 1ms, T_{exc} = 5ms$): (a) 2-photon process with 980nm excitation. (b) 3-photon process with 1550nm excitation.....	13
Figure 7. Measured emission intensity of aUCNPs at different power levels: (a) 2-photon process with 980nm excitation. (b) 3-photon process with 1550nm excitation.	14
Figure 8. Excited concentrated aUCNP vial image: (a) vial and emission beam photograph. (b) acquired time-resolved image ($T_{exc} = 5ms, T_{int} = 10ms$).....	16
Figure 9. Single PDMS micro-well structure image: (a) micro-well photograph. (b) acquired image (66 W/cm ² of 1550nm excitation)	17
Figure 10. Closely-spaced micro-wells image in PDMS structure: (a) micro-wells photograph. (b) acquired image (66 W/cm ² of 1550nm excitation)	18
Figure 11. aUCNP-injected mammary fat pad emission over 6 hours. (images in counts/sec and obtained using the IVIS imager).....	19
Figure 12. aUCNP-injected mammary fat pad emission spectrum (images obtained using the IVIS imager): (a) left side (injected) and right side (non-injected) IVIS images. (b) left and right side emission spectrum.....	20

1 Introduction

1.1 Motivation

Treatment of cancer with surgery and radiation relies heavily on the ability to both localize and quantify tumor cell distribution to direct where the treatment should be focused; however, this information is not presently available for microscopic tumor foci leaving physicians to empirically treat wide areas of tissue, causing significant toxicity, or risk leaving untreated tumor cells behind, worsening cancer outcomes. While gross ($>1\text{cm}$) tumor is detectable by eye and touch, microscopic residual disease (MRD) consisting of clusters 100s and 1000s of tumor cells morphologically similar to their normal tissue counterparts, cannot be readily visualized. The ability to precisely identify, localize and quantify the spread of the tumor cells during surgery is paramount to the successful outcome of the operation and, if necessary, post-operative radiation. Failure to properly resect and remove residual tumor around the periphery of tumor cavities dramatically increases the risk of cancer recurrence, for example in breast cancer doubling the risk

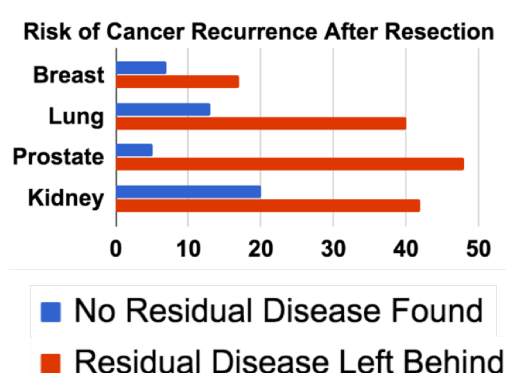


Figure 1. Effects of MRD on cancer recurrence rates.

of recurrence from 15% to 30% over a span of 10 years [1]. Figure 1 demonstrates the stark increase in cancer recurrence rates for several types of cancers in cases where microscopic residual disease was left behind during surgery. Once MRD has been assessed to have been left behind, it either necessitates a re-excision of the MRD or an acceptance of a higher risk of recurrence and death from cancer. Alternative strategies center around empirically removing an excessive amount of healthy tissue. A similar challenge occurs in prostate cancer where up to 50% of high risk prostate cancer patients are found to have MRD post-operatively and must undergo 8 weeks of radiation and hormone therapy.

Despite the lack of a practical intraoperative imager, surgeons have tried to find other ways to identify microscopic residual disease or assess whether or not disease is left behind during surgery, but nearly all of the current methods require a significant amount of post-surgery lab analysis and the results often are too late to be useful. Current strategies for MRD detection rely on examining excised tissue labeled with highly specific cancer markers under a microscope, post-operatively. However, tissue processing, staining and microscopic evaluation of the excised tissue surface (which, by proxy, connotes the presence or absence of residual tumor on the corresponding area within the patient) restricts MRD evaluation to the post-operative pathology lab, taking days to weeks to return a result. This latency hinders the treatment process and compromises the success of the initial resection surgery in more than 25% of the cases, requiring additional surgical operations along with other forms of treatments such as irradiation, or chemotherapy. An efficient and practical intraoperative imaging platform is therefore an evident need for the successfulness of cancer treatment surgeries.

1.2 Challenges

Current intraoperative imaging apparatuses are too rigid, bulky and insensitive due to their requirement for complex optics and filters. An ideal and practical intraoperative imager needs to be sensitive enough to be able to detect microscopic disease in real-time during resection surgery and provide a visualization of tumor foci in the tumor cavity for the clinicians, and additionally, have a small form factor and be compatible with clinical and surgical instruments often used during operations.

Attempts at intraoperative image guidance continue to fail for MRD detection due to the bulk and rigidity of the required optics and filters. To help with identifying the extent and boundaries of the tumor and determining whether or not further resection of the tumor cavity and draining lymph nodes is necessary, current technologies leverage fluorescently tagged biomarkers engineered to specifically attach to cancer cells, coupled with intraoperative imagers to visualize where the disease is present. Such an image resolution method requires optical filters which adds to the bulkiness of the overall imager and probe. Optical filters are required to reject excitation light which is often 4-6 orders of magnitude stronger than the weak, only-50nm shifted fluorescent emission light, and autofluorescence remains a persistent problem. In addition to that, focusing optics are required to maintain spatial resolution and precisely guide the excitation and emission

light through the optical system. These filters and lenses confer a size and rigidity impractical for a complete examination of the tight confines of modern minimally invasive tumor cavities or lymph node basins[2]. Furthermore, size-constrained to operate outside the tumor bed, far from the tissue, optical sensitivity is dramatically reduced.

1.3 Objectives

This work presents a new strategy to move the cumbersome imaging requirements imposed by wavelength selective imaging to a time domain, inherently compatible with CMOS. Enabled by uniquely efficient alloyed upconverting nanoparticles (aUCNPs) [3], with long luminescent life-times, up-conversion of light, and visualization at light intensities compatible with *in vivo* use, presented here is an imaging platform freed from the need for optical filters and lenses, capable of being placed directly on the tissue surface, increasing sensitivity due to proximity to cells. Furthermore, spatial resolution is achieved using a combination of proximity and angle-selective gratings[4][5], integrated directly on chip. The resultant IC-only imager can be thinned to a negligible thickness nearing only $25\mu m$, enabling a flexible scalable, molecular imaging skin, capable of being integrated on any surface.

2 Fluorescence Imaging

Fluorescence imaging is based on the fact that biomarkers and fluorescent molecular tags, along with proper antibodies, can provide very accurate and reliable binding to cancer cells and provide a contrast between healthy and cancerous regions. Once attached to cancer cells, the molecular markers can be excited with a suitable excitation light source and the emission, once collected, captured and resolved, can provide us with the visualization of any microscopic cancer cell residuals. Figure 2 represents how this process works.

When it comes to fluorescence imaging, there are two main approaches; frequency domain, and time domain image resolution. Each one differs in the way the excitation and emission light are respectively applied and extracted from the sea of signals generated around the sample.

2.1 Frequency domain resolution

2.1.1 Concept

Frequency domain resolution takes advantage of the fact that the emission coming from any fluorescent marker has in fact a different wavelength than the excitation light to which the particle reacts to and absorbs. This shift in wavelength, which more so than often results in a longer emission wavelengths due to intrinsic losses in atomic transitions and photon generation, is not significant, and therefore, the wavelength difference is only subtle. This small difference in the wavelength of emission light however, allows optical filters to separate and extract the emission signal from the excitation light.

2.1.2 Challenges

Frequency domain image resolution is heavily dependent on the accuracy and efficiency of the optical filter being used. The higher the rejection of the excitation light is, the better the signal-to-background ratio of the resulting image will be. Moreover, these optical filters will need to have an extremely narrow and sharp transition band to be able to separate two very closely spaced wavelengths, and will also have to be angle-insensitive to be able to let through the entire emission light emanating from the molecular markers. In addition to what has been mentioned, the

filter will eventually need to achieve 4-6 orders of magnitude of rejection to be able to extract the very weak emission signal from the much stronger excitation light. The combination of all of these stringent requirements and specifications for the optical filter makes frequency domain imagers bulky, cumbersome and unable to achieve small form factors, and thus, are not practical solutions for intraoperative imagers.

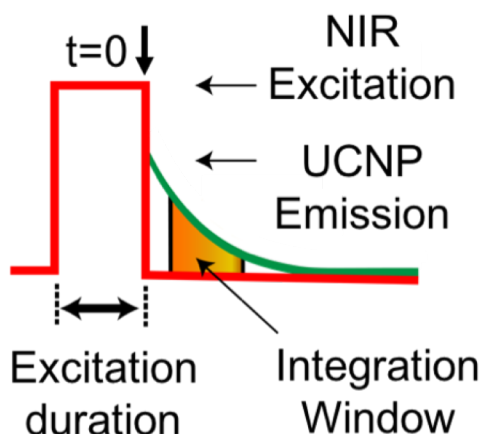


Figure 2. Time domain image resolution diagram.

2.2 *Time-domain resolution*

Every phenomenon at the atomic level requires some finite amount of time to be fully carried out. Atomic transitions and photon generation and release are no exception. Such transitions require a given amount of time in which the electrons absorb the incoming excitation photon and release it back, generating the emission light as a result. As a consequence, if the excitation light suddenly turns off, the emission light will still persist for a short amount of time afterwards, which makes time-domain image resolution possible.

2.2.1 *Concept*

Unlike frequency domain resolution, time domain image resolution does not rely on wavelength or frequency features of the excitation and the emission light. Instead, it is based on a time domain separation and extraction of the two lights, alleviating the need for any frequency-selective optical filter. In simpler terms, in order for the excitation light not to interfere with the capturing of the emission signal, the excitation light is turned off during the image resolution

process, no longer necessitating an optical filter to reject and block the interfering excitation light. The remaining emission signal is then collected and captured by the sensor.

2.2.2 Challenges

The main challenge with a time-domain image resolution technique is the fact that most of the conventional fluorophores and molecular markers available have a very short emission lifetime, which imposes an extremely heavy burden on the speed of the image sensors being used with those particles. With a lifetime of only a few nanoseconds, the sensor and required circuitry would need to operate at a significantly higher speed than conventional silicon sensors are capable of. In addition, care should be taken that the excitation light does not interfere with the normal course of operation of the silicon imager and compromise the signal-to-background ratio. To this aim, our proposed platform incorporates alloyed upconverting nanoparticles to replace conventional fluorophores and allow us to carry out time gated imaging without burdensome speed requirements imposed on the imager array.

3 Alloyed Upconverting Nanoparticles

Alloyed UCNPs, unlike conventional fluorescent markers, are capable of sustaining an emission in the visible range, while being excited in the near-infrared (NIR) range [6][7]. The three particles that we are investigating in this work have NaYbErF₄ as their core, but at three different composition ratios of Yb/Er; 20/80, 60/40 and 80/20. Yb is the main photon- absorbent at 980nm, while Er is responsible for absorption at 1550nm, where 980nm and 1550nm are the two excitation wavelengths for a 2- and 3-photon process respectively. All three aUCNPs have 8nm sized core, with 4nm sized shells of NaYF₄ with 20% Gd, diluted to a concentration of 0.68uM in Hexane. A negative control and reference is also measured for each experiment using a Hexane-only solution.

Specifically engineered and with the correct linker molecule and antibody, they can bind to tumor cells allowing greatly enhanced selectivity compared to non-specific biomarkers. In this work, in order to demonstrate initial realization and implementation of this imaging method, we have only used unaltered aUCNPs without tumor-specific binding agents.

To quantify and compare the three different composition of aUCNPs, we have measured their power efficiency, emission lifetime and intensity using our custom-made CMOS imager, at both absorption wavelengths (980 and 1550nm). A vial containing 400uL of the 0.68uM aUCNP solution is placed directly above the imager array, and the solution is then illuminated (excited) with the corresponding time-gated collimated laser beam. Figure 3 depicts the experiment setup for these measurements.

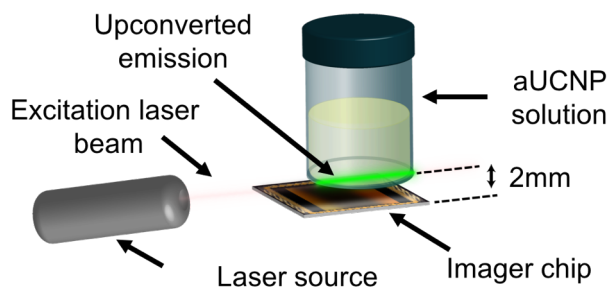


Figure 3. Experiment setup for aUCNP characterization.

The three main factors contributing to the ultimate efficiency of the aUCNPs for clinical application are power conversion efficiency, emission lifetime and the duration of excitation required[8].

3.1 Emission decay

To obtain the emission decay lifetime, we can reproduce a representation of the decay profile using a moving integrating window, easily realizable with the custom-made imager. As derived in [8], the measured photocurrent will be as follows:

$$I_A(t) = I_{A_0} e^{(-\frac{t}{\tau})} + I_D$$

where τ and I_D are respectively the emission decay lifetime and dark current level in the pixels. Figure 4(a) and (b) show the measured emission decays for the three aUCNPs and the negative control, at 980nm and 1550nm excitation respectively. The dark current level is subtracted from the waveform for visual purposes. The data points have been obtained using a moving but fixed-length integration window of 1ms.

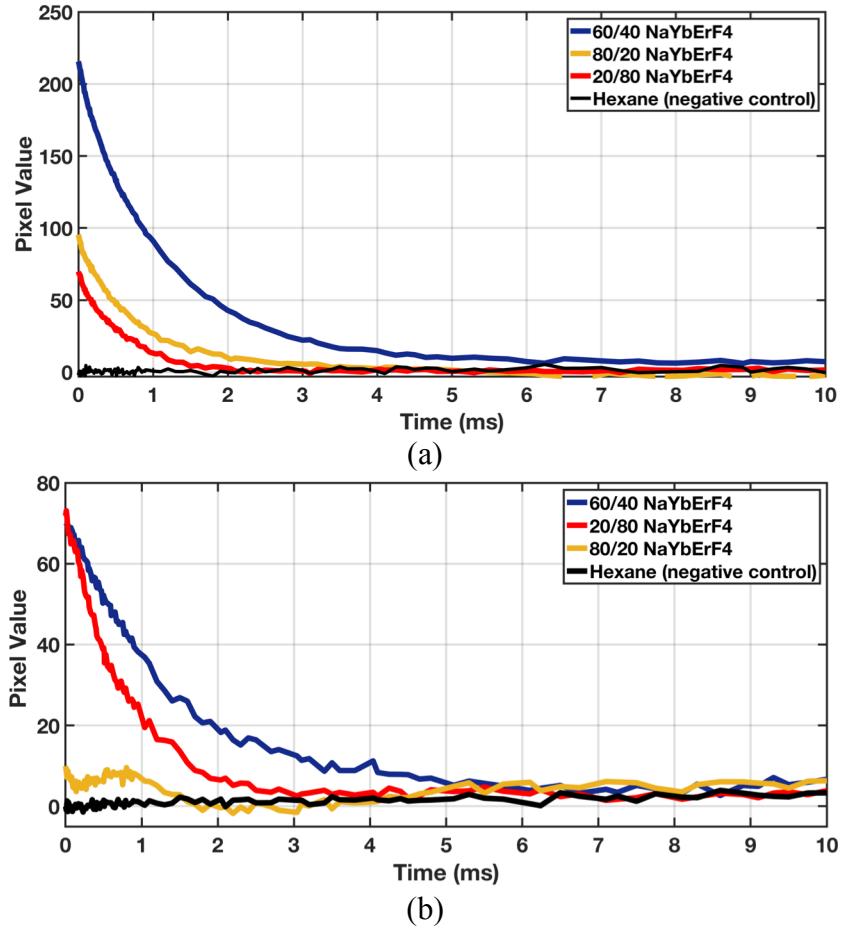


Figure 4. Measured emission intensity decay of aUCNPs (dark current subtracted and $T_{exc} = 5$ ms): (a) At 8 W/cm² of 980nm excitation. (b) At 60 W/cm² of 1550nm excitation.

The emission decay profiles obtained at 1550nm excitation visibly show that compared to the 980nm-excited 2-photon process, the 3-photon process is approximately 22 times less brighter.

Keeping in mind that Silicon's bandgap energy corresponds to a wavelength of 1103nm[9], despite the apparently poorer upconversion of a 3-photon process, the overall efficiency of the imaging system can be higher, owing to the fact that a 1550nm excitation source will introduce negligible interference on the Si-based CMOS circuit compared to its 980nm counterpart. Using higher excitation powers at 1550nm to compensate for the smaller upconversion rate will ultimately lead to a higher image quality, and mainly a higher signal-to-background ratio.

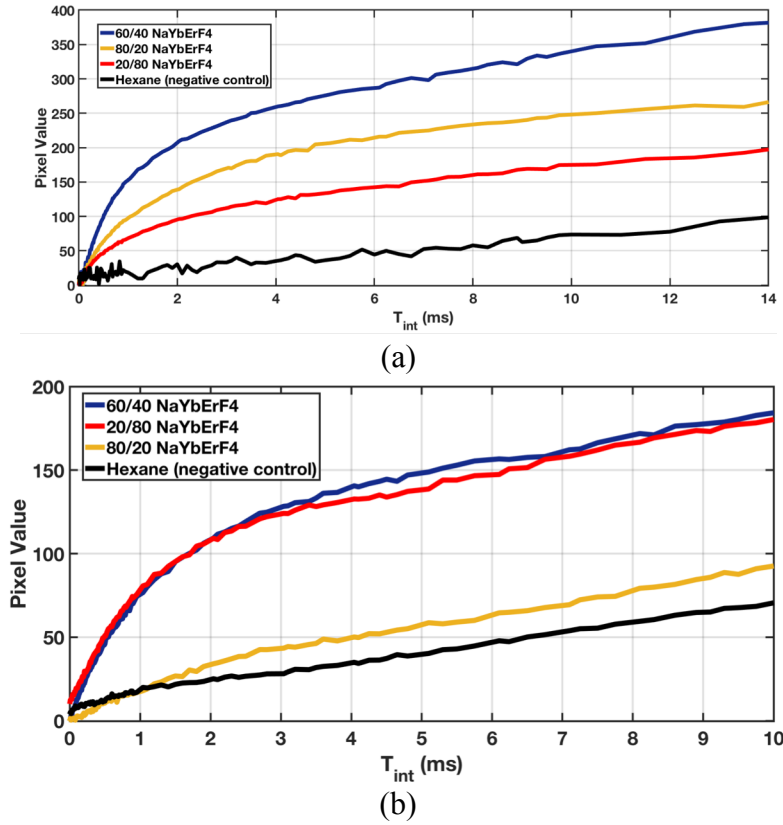


Figure 5. Measured integrated emission intensity of aUCNPs ($T_{exc} = 5\text{ms}$): (a) At 8 W/cm² of 980nm excitation. (b) At 60 W/cm² of 1550nm excitation.

Another quite useful way of comparing the intensity of the three aUCNPs is to look at the integrated emission intensity, that is the total measured signal level at different integration window lengths. Figure 5(a) and (b) illustrate these results. Derived in [8], the obtained results can be expressed as

$$I_B(t) = I_{B_0} \left[1 - e^{(-\frac{t}{\tau})} \right] + i_d t$$

where I_{B_0} , τ and i_d are respectively a constant, the emission decay lifetime and the dark current intensity. The end slope of this equation represents the dark current which can also be observed in all the plots in Figure 4. As shown in Figure 4, the Hexane negative controls have the lowest pixel

values, and given the absence of any aUCNPs, their measured integrated signal is a sloped line with no exponentially decaying component.

3.2 Upconversion efficiency

To characterize the upconversion efficiency of the aUCNPs, we have measured the upconverted emission at different power intensities. The measured emission intensities are plotted in Figure 6. The measurements have been conducted at both excitation wavelengths and compared with respect to the Hexane negative control.

The upconverted emission is measured to be quite linear with the input excitation power, for both the 2- and 3-photon process. At the relatively lower powers where the measurements are

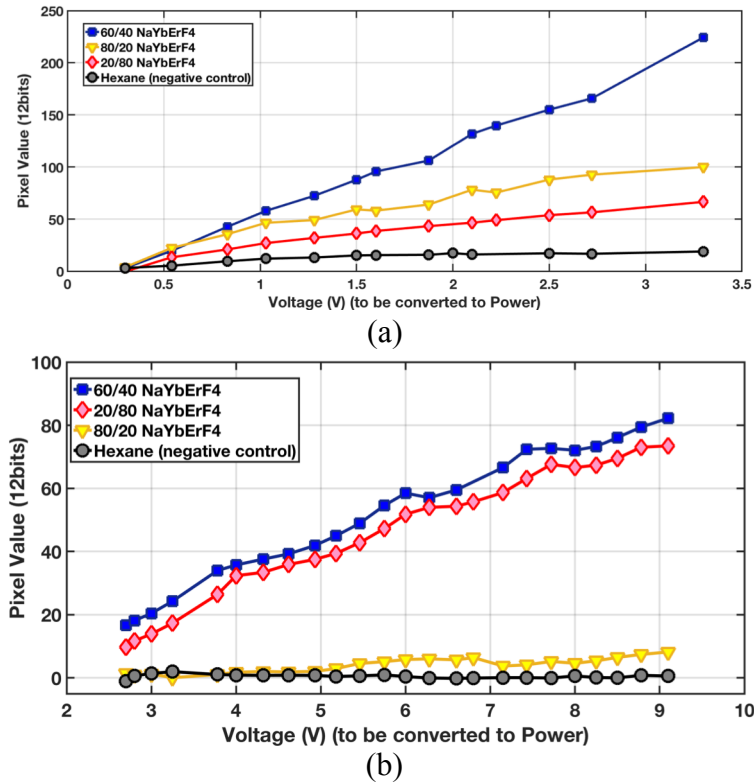


Figure 6. Measured emission intensity of aUCNPs at different power levels ($T_{int} = 1ms, T_{exc} = 5ms$): (a) 2-photon process with 980nm excitation. (b) 3-photon process with 1550nm excitation.

conducted at, the output flux of emission photon is, to first order, linearly proportional to the input flux. Higher power levels may lead to secondary order non-linearities which are not applicable and relevant to our case.

Comparing the data for the two processes in Figure 6, it can be seen that the 980nm light produces a small amount of interference, reflected in the Hexane negative control plot. This interference is generated through the scattering of the excitation laser beam onto the Si-based imager, resulting in an undesired increase in the background level. However, such an interfering effect is almost negligible and not visible in the measurements, as seen in Figure 6(b).

3.3 Excitation duration

Another contributing element to the signal intensity is the duration of excitation, T_{exc} , which represents how long the nanoparticles are illuminated with the excitation light source before

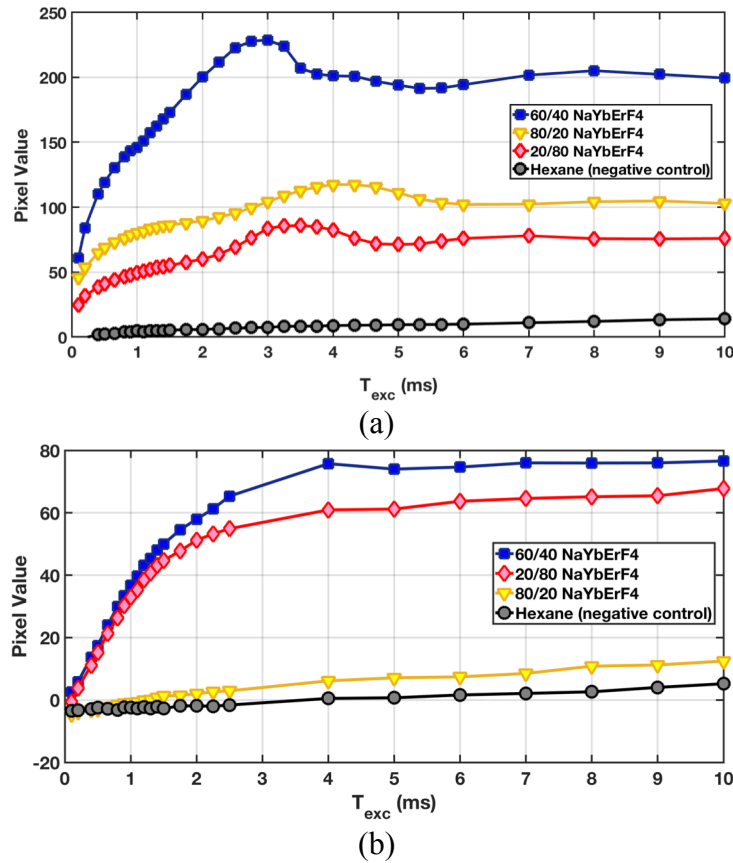


Figure 7. Measured emission intensity of aUCNPs at different power levels:

(a) 2-photon process with 980nm excitation. (b) 3-photon process with 1550nm excitation.

the start of the time-gated imaging sequence. The aUCNPs were excited for various durations of time (T_{exc}) and the measured emission intensities are brought in Figure 7(a) and (b) for 980nm and 1550nm excitation respectively. It can be seen from the plots in Figure 7 that there is a noticeable increase in the emission in all three aUCNPs, until T_{exc} reaches a point after which no significant increase is observed. For our work, we have used a 5ms illumination time for our experiments

($T_{exc} = 5\text{ms}$). It should be noted that being externally driven with a synchronized pulse stream, the excitation laser power is susceptible to any transient non-idealities in the pulse waveform, i.e. ringing, as seen in Figure 7(a).

4 Imaging Platform and Experimental Image Acquisition

In order to validate the proof of concept for this imaging system, we have devised two sets of experiments to acquire time-gated images from various structures containing or coated with aUCNPs to characterize the spatial resolution and detection threshold of our imager with the described illumination scheme. The first experiment includes imaging of a glass vial containing a solution of aUCNPs directly placed on the chip, and the second experiment was conducted with custom-made three dimensional micro-wells fabricated in PDMS, and then later coated with aUCNPs.

4.1 Concentrated aUCNP vial

In this experiment, a vial containing 400 μ L of aUCNP solution (60/40 NaYbErF₄) at a concentration of 0.68 μ M is sealed and placed in close proximity to the imager, sitting at only 2mm distance. As shown in Figure 3, the vial is then excited with a collimated excitation beam with a 980nm laser source, creating a corresponding emission beam within the solution. The emission beam is subsequently captured and acquired by the imager. The illumination method scheme used here is a time-gated excitation, and the image is acquired using the time-domain image resolution method previously described. Figure 8 shows the resulting image obtained after acquisition.

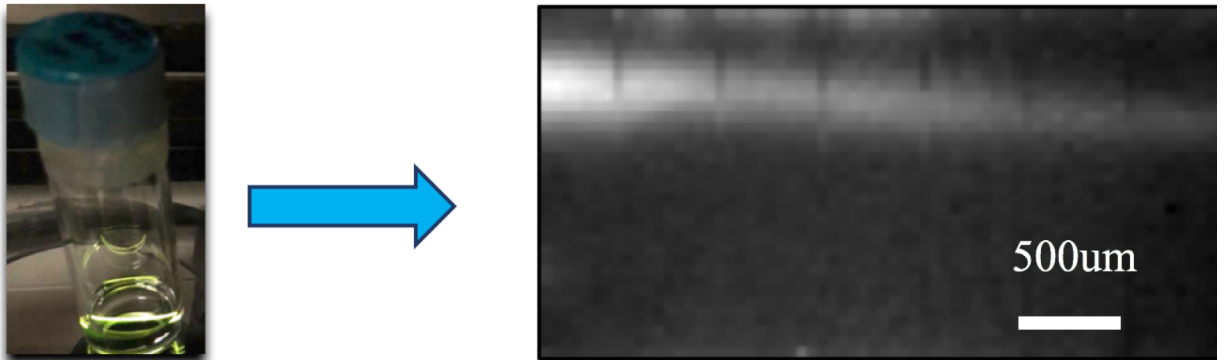


Figure 8. Excited concentrated aUCNP vial image: (a) vial and emission beam photograph. (b) acquired time-resolved image ($T_{exc} = 5ms, T_{int} = 10ms$)

4.2 *aUCNP-coated Polydimethylsiloxane (PDMS) Micro-well*

To assess the spatial resolution and accuracy of this platform, we created micro-structures fabricated in PDMS and used cell-level sized structures to replicate residual tumor cell clusters in real life. We fabricated two sets of micro-wells and coated their internal surface with 5pM/mm² of aUCNP. The wells are square-shaped and their dimensions are 500×500×500(L×W×H)(μm).

The first structure is a single well whereas the second one has two closely spaced replicas of the first individual well to assess the resolution of the imaging chip in a time-gated image acquisition technique. The spacing between the two wells in the second structure is 0.25mm, and considering that each cell measure around 10μm (length, width and height), each well area translates into approximately 2000 cells and with the spacing between the two well, the distance between the two micro-structure is only 25 cells, which is enough precision for a guided resection surgery. In this experiment, we have used a 1550nm excitation source to illuminate and excite the aUCNP-coated microstructures, and taken advantage of the fact that Silicon is insensitive to the 1550nm wavelength, which no longer restricts us to use a time-domain image resolution.

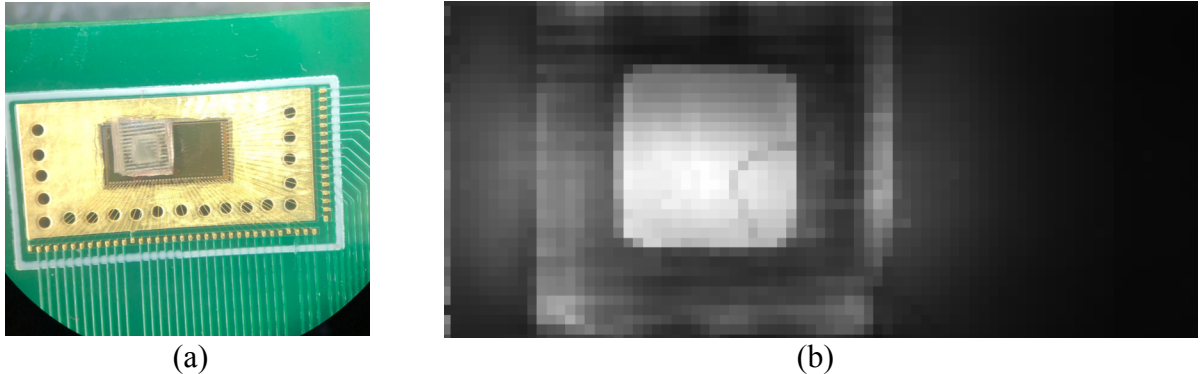


Figure 9. Single PDMS micro-well structure image: (a) micro-well photograph. (b) acquired image (66 W/cm^2 of 1550nm excitation)

The first part of this experiment includes the single-well and Figure 9 shows the single micro-well photograph placed on the imager array, and the corresponding acquired image. From the image seen in Figure 9 (b), we can very clearly and distinctively visualize the well, which mimics the cancer cells, from the surrounding background, which represents the surrounding tissue in the body. However, the main and major feature of intraoperative imagers that can help improve the success rate of resection surgery, is the spatial resolution and the ability to detect closely spaced clusters of cancer cells among healthy ones.

To that aim, we conducted another experiment that included the second set of the custom-fabricated PDMS structures. A pair of closely spaced micro-wells would imitate a very common scenario during surgery where two clusters of cancer cells are located within a very short distance of each other and separated by healthy cells in between. The goal of every resection surgery is to minimize morbidity and loss and resection of healthy tissue, therefore it is surgically very crucial to be able to determine with high accuracy if there is healthy tissue among closely spaced cancer cells. Figure 10 shows the result of this experiments on the micro-well structure. The resulting image acquired illustrates that the two wells, despite being separated by only $250\mu\text{m}$, are still very clearly distinguishable and that consequently, the performance of this imager array is nominally acceptable for surgical and medical procedures.

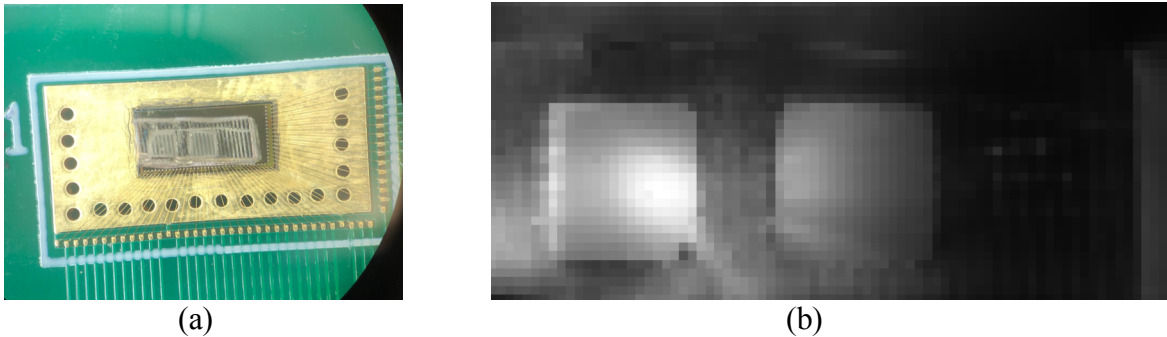


Figure 10. Closely-spaced micro-wells image in PDMS structure: (a) micro-wells photograph. (b) acquired image (66 W/cm^2 of 1550nm excitation)

5 Animal Trial and Bio-distribution

To observe bio-distribution, toxicity and sentinel lymph node identification, we grew breast HER2+ breast tumors in 6 mice and once mature and ready, we conducted intratumoral injections of the nanoparticles into the mammary fat pads of the mice. The mice were later individually sacrificed at 6 different time-points and the injected mammary glands were imaged with IVIS spectrum imager (PerkinElmer) with an excitation power of $0.1\text{W}/\text{cm}^2$ (at a wavelength of 980nm)[10]. Figure 11 shows the measured intensity of the emission of the nanoparticles injected into the mammary fat pad of one of the mice over a period of 6 hours, where we measured the emission every 2 hours. Despite the slight intensity decrease observed in Figure 11, the particles still remain in the gland even hours after injection, which is enough time to allow surgeons to conduct a complete guided resection surgery of a breast tumor.

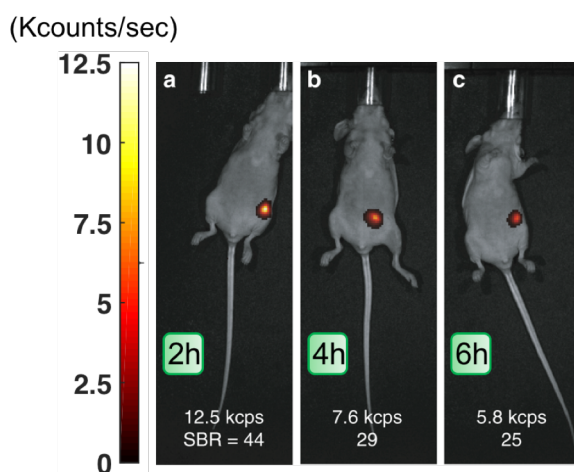


Figure 11. aUCNP-injected mammary fat pad emission over 6 hours. (images in counts/sec and obtained using the IVIS imager)

As a negative and reference control, and to ensure that our IVIS images are in fact capturing the emission of the aUCNPs and that no autofluorescence or other source of potential interference is being misinterpreted, we have measured the spectrum of the emission from the injected and non-injected mammary fat pad, and the resulting spectrums are illustrated in Figure 12. Knowing that the aUCNPs emit in the 550nm and 660nm range, based on the spectrum obtained, we can

definitively assert that the signal being observed is in fact from the aUCNP and surrounding healthy tissue and cells do not produce any source of interference or autofluorescence.

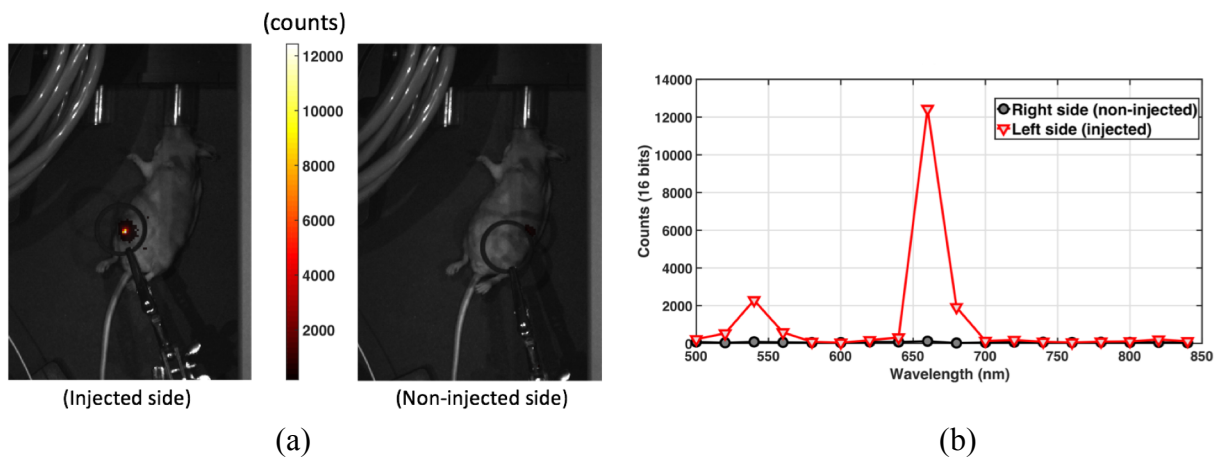


Figure 12. aUCNP-injected mammary fat pad emission spectrum (images obtained using the IVIS imager): (a) left side (injected) and right side (non-injected) IVIS images. (b) left and right side emission spectrum.

6 Future work and conclusion

This work aimed at providing a novel imaging platform to allow intraoperative integration of reasonably acceptable precision imagers for microscopic residual disease detection during surgery and therefore, greatly improve the speed and success of resection surgeries. We demonstrated a proof of concept for our proposed method using a Silicon-based imager array and leveraged inorganic lanthanide-based nanoparticles and their long emission lifetimes to be able to acquire the image in time-domain and use a time-resolved imaging technique and as a result, eliminate the need for bulky and cumbersome optics and filters that prevented true and full integration of intraoperative imagers onto surgical instruments.

We were able to imitate cell-cluster-level approximations of the conditions in the body to put the spatial resolution of our imaging platform to test and were able to obtain surgically acceptable precisions using tissue-imitating micro-wells in PDMS structures.

Future works will aim to include enhanced pixel amplifier and optimally sized and designed imager array, alongside the improvement of aUCNP emission signal intensity and power efficiency and better responsivity and binding ratio to cancer cells

Bibliography

- [1] H. Bartelink, et al., “Recurrence rates after treatment of breast cancer with standard radiotherapy with or without additional radiation,” *New England J. of Medicine*, vol. 345, no. 19, pp. 1378-1387.
- [2] N. Tagaya, R. Yamazaki, A. Nakagawa, A. Abe, K. Hamada, K. Kubota, and T. Oyama, “Intraoperative identification of sentinel lymph nodes by near-infrared fluorescence imaging in patients with breast cancer,” *The American Journal of Surgery*, vol. 195, no. 6, pp. 850 – 853, 2008.
- [3] S. Wilhelm, “Perspectives for upconverting nanoparticles,” *ACS Nano*, vol. 11, no. 11, pp. 10644–10653, 2017, pMID: 29068198.
- [4] E. P. Papageorgiou, B. E. Boser, and M. Anwar, “Chip-scale fluorescence imager for in vivo microscopic cancer detection,” in *2017 Symposium on VLSI Circuits*, June 2017, pp. C106–C107.
- [5] E. P. Papageorgiou, B. E. Boser, and M. Anwar, “An angle-selective CMOS imager with on-chip micro-collimators for blur reduction in near-field cell imaging,” in *2016 IEEE 29th International Conference on Micro Electro Mechanical Systems (MEMS)*, Jan 2016, pp. 337-340.
- [6] E. M. Chan, E. S. Levy, and B. E. Cohen, “Rationally designed energy transfer in upconverting nanoparticles,” *Advanced Materials*, vol. 27, no. 38, pp. 5753–5761.
- [7] A. D. Ostrowski, E. M. Chan, D. J. Gargas, E. M. Katz, G. Han, P. J. Schuck, D. J. Milliron, and B. E. Cohen, “Controlled synthesis and single-particle imaging of bright, sub- 10 nm lanthanide-doped upconverting nanocrystals,” *ACS Nano*, vol. 6, no. 3, pp. 2686–2692, 2012, pMID: 22339653.
- [8] Najafiaghdam, Hossein, et al. "A Molecular Imaging “Skin A Time-resolving Intraoperative Imager for Microscopic Residual Cancer Detection Using Enhanced Upconverting Nanoparticles." 2018 40th Annual International Conference of the IEEE Engineering in Medicine and Biology Society (EMBC). IEEE, 2018.

- [9] M. A. Green, J. Zhao, A. Wang, P. J. Reece, and M. Gal, “Efficient silicon light-emitting diodes,” *Nature*, vol. 412, no. 6849, pp. 805–808, Aug. 2001.
- [10] Tian, Bining, Angel Fernandez-Bravo, Hossein Najafiaghdam, Nicole A. Torquato, M. Virginia P. Altoe, Ayelet Teitelboim, Cheryl A. Tajon, et al. “Low Irradiance Multiphoton Imaging with Alloyed Lanthanide Nanocrystals.” *Nature Communications* 9, no. 1 (August 6, 2018)